# Defect Contrast with 4D-STEM: Understanding Crystalline Order with Virtual Detectors and Beam Modification

Stephanie M Ribet, Colin Ophus, Roberto dos Reis, Vinayak P Dravid



**Original Article** 



## Defect Contrast with 4D-STEM: Understanding Crystalline Order with Virtual Detectors and Beam Modification

Stephanie M. Ribet<sup>1,2,3</sup>, Colin Ophus<sup>3</sup>, Roberto dos Reis<sup>1,2,4</sup>,\*, and Vinayak P. Dravid<sup>1,2,4</sup>,\*

#### **Abstract**

Material properties strongly depend on the nature and concentration of defects. Characterizing these features may require nano- to atomic-scale resolution to establish structure–property relationships. 4D-STEM, a technique where diffraction patterns are acquired at a grid of points on the sample, provides a versatile method for highlighting defects. Computational analysis of the diffraction patterns with virtual detectors produces images that can map material properties. Here, using multislice simulations, we explore different virtual detectors that can be applied to the diffraction patterns that go beyond the binary response functions that are possible using ordinary STEM detectors. Using graphene and lead titanate as model systems, we investigate the application of virtual detectors to study local order and in particular defects. We find that using a small convergence angle with a rotationally varying detector most efficiently highlights defect signals. With experimental graphene data, we demonstrate the effectiveness of these detectors in characterizing atomic features, including vacancies, as suggested in simulations. Phase and amplitude modification of the electron beam provides another process handle to change image contrast in a 4D-STEM experiment. We demonstrate how tailored electron beams can enhance signals from short-range order and how a vortex beam can be used to characterize local symmetry.

Key words: 4D-STEM, defects, phase plate, vortex beam

#### Introduction

The presence of defects disproportionately impacts the electronic and crystal structures of materials giving rise to many useful properties. As a consequence, the ability to identify and control the concentration and nature of defects has been explored for many years. For example, impurities in silicon change its electronic properties allowing for the development of solid-state devices (Jacoboni et al., 1977). Defects at multiple length scales are known to enhance phonon scattering for more efficient heat conversion in thermoelectric systems (Zheng et al., 2021). Dislocations and grain boundaries play a key role in plastic deformation and resulting mechanical properties (Van Swygenhoven & Weertman, 2006). In nanocomposite materials, the topology and interfaces of dissimilar components strongly influence the structure-property relationships in these systems (DiStefano et al., 2020; Ribet et al., 2021). Understanding defects and their impact on material properties is essential for technological development.

The presence of defects breaks long-range order in materials, which is reflected in local symmetry (Zeng et al., 2011; Sun et al., 2014; Liu et al., 2022). There are a variety of ways to characterize order ranging from bulk scale property measurements capturing ensemble behavior to atomic resolution imaging to identify individual structural changes (Araujo et al., 2012). It is often important to reach nanoto atomic-scale resolution to establish form-function relationships, and the small probe size of scanning transmission electron microscopy (S/TEM) makes it a useful tool to study these features. Improvements in aberration correction of electron microscopes have led to the wide availability of

sub-angstrom probe sizes that can be used for atomic resolution defect detection in many materials (Dahmen et al., 2009; Krivanek et al., 2010).

In addition to traditional real space imaging approaches, local structural order can be probed by recording electron diffraction patterns. A convergent beam electron diffraction (CBED) pattern recorded in STEM reflects structural information about the area illuminated by the electron beam. In 4D-STEM or scanning diffraction experiments, a CBED pattern is recorded at each position defined in real space (Fig. 1a). These experiments have more recently been propelled forward thanks to the wide introduction of fast, pixelated direct electron detectors. One benefit of a 4D-STEM approach is the remarkable versatility in image reconstruction. For both experimental and simulated data, any mask can be applied as a virtual detector in postprocessing or even during the experiment (Plotkin-Swing et al., 2022), whereas conventional imaging approaches rely on binary detectors of fixed geometry. By collecting these large datasets and processing with virtual detectors, 4D-STEM can map material structure and properties not available in conventional experiments (Ophus, 2019).

There are many methods for signal enhancement in electron microscopy images to help probe local defects. In annular dark-field (ADF) STEM images, the contrast is sensitive to atomic number and thickness (Krivanek et al., 2010). These scattering cross sections can be used in physics-based models to find atomic positions even for sparse data (Fatermans et al., 2018). Dark-field-based atomic counting algorithms are also sensitive to thickness and can be used for 3D material

<sup>&</sup>lt;sup>1</sup>Department of Materials Science and Engineering, Northwestern University, Evanston, IL, USA

<sup>&</sup>lt;sup>2</sup>International Institute of Nanotechnology, Northwestern University, Evanston, IL, USA

<sup>&</sup>lt;sup>3</sup>National Center for Electron Microscopy, Molecular Foundry, Lawrence Berkeley National Laboratory, Berkeley, CA, USA

<sup>&</sup>lt;sup>4</sup>The NUANCE Center, Northwestern University, Evanston, IL, USA

<sup>\*</sup>Corresponding author: Roberto dos Reis, E-mail: roberto.reis@northwestern.edu; Vinayak P. Dravid, E-mail: v-dravid@northwestern.edu

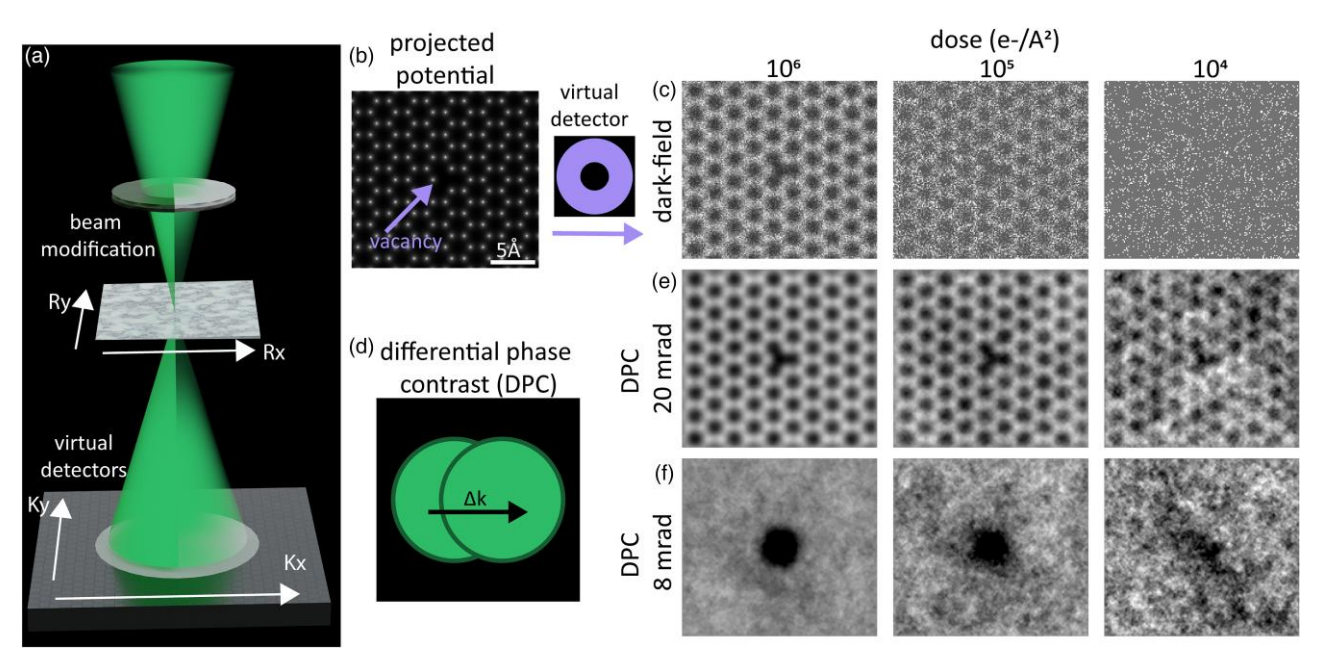


Fig. 1. (a) 4D-STEM schematic showing virtual detectors and beam modification. (b) Simulated potential of graphene with a vacancy. (c) Dark-field imaging is not dose efficient. (d) DPC can be used to recover the phase as shown in (e,f). A larger converge angle (e) provides atomic resolution contrast, while a smaller convergence angle (f) shows a stronger signal from the missing atom.

characterization including recovery of defects (Arslan Irmak et al., 2021; Van Aert et al., 2011). Neural-network-based deep learning analytical methods can be applied to characterize and retrieve material structural information with improved reliability and throughput (Ziatdinov et al., 2017; Madsen et al., 2018). Denoising algorithms, such as finding low-rank representations of the data, can improve signals from defects (Zhang et al., 2020), especially in multidimensional datasets and in some cases also in individual images (Spiegelberg et al., 2018). Finally, more complex algorithms for multidimensional datasets, such as rotationally invariant variational autoencoders, can be used for enhancing signals and finding defects in materials (Oxley et al., 2021).

Despite improvements in hardware, software, and algorithms, there are still significant challenges in direct defect detection, especially when characterizing soft and hybrid materials (Chen et al., 2020; Bustillo et al., 2021; Ribet et al., 2021). These systems tend to be beam sensitive and may not withstand higher electron doses that are needed to resolve atomic features (Egerton & Watanabe, 2022). Even with the improvement in the dynamic range of direct electron detectors (Tate et al., 2016; Haas et al., 2021; Philipp et al., 2022; Plotkin-Swing et al., 2022), it can be challenging to capture weakly scattered signals. Therefore, we seek approaches that efficiently highlight defective sites and related symmetry information, without the need for atomic resolution studies. Easy defect detection can be useful for rapid characterization of materials and for intelligently informing microscopy parameters in on-the-fly experiments. Moreover, there can be ambiguity about whether defects are inherent to the sample or caused from beam-specimen interactions, making it attractive to detect defects at lower doses.

Graphene, a two-dimensional structure, has attracted great attention due to its remarkable physical and electronic properties (Geim & Novoselov, 2007). Structural defects strongly influence graphene's performance and significant efforts have

been devoted to characterizing them at multiple length scales with both spectroscopic and imaging techniques (Araujo et al., 2012). Graphene is an ideal model system for testing the impact of beam modification and virtual detectors on 4D-STEM experiments. The simple scattering inherent to its two-dimensional nature makes it more straightforward to understand the origin of contrast in images. Moreover, graphene is the quintessential example of a weak phase object, meaning that it does not impart a large phase shift on the initial probe. In order to achieve reasonable contrast, especially for atomic resolution imaging, a high electron dose needs to be applied. The knock-on threshold for graphene is 86 kV (Smith & Luzzi, 2001), so a number of S/TEM studies have been able to image this structure at atomic resolution at or below the damage threshold (Dahmen et al., 2009; Huang et al., 2011; Ophus et al., 2015; Ziatdinov et al., 2017; Ishikawa et al., 2018; Madsen et al., 2018; O'Leary et al., 2021a). These studies can serve as a benchmark for our work, as we search for efficient defect detection schemes, which can be extended to less robust materials.

We first consider the application of virtual detectors to recover bright-field (BF) and ADF images in our model case of graphene with a vacancy (Fig. 1b). As seen in Figure 1c, ADF imaging needs a relatively large number of electrons (> $10^4e^-$  Å<sup>-2</sup>) to yield an acceptable contrast to directly visualize the atomic positions. BF imaging shows a lower dose efficiency in this case (Supplementary Fig. S1). Moreover, these images were formed with the most ideal experimental conditions, namely an aberration-free probe and a large convergence angle (20 mrad). The true resolution will be set by a balance between aberrations and the diffraction limitations of the convergence angle. Therefore, we seek a dose-efficient reconstruction method and a technique to highlight important signals derived from defective areas, even in resolution-limited cases.

For weakly scattering samples, phase contrast imaging approaches, such as differential phase contrast (DPC) or

ptychography, lend themselves well to accurately recovering the object signal. The intensity distribution in the electron probe is shifted when it interacts with local variation in the sample potential, leading to a change in the center of mass of the transmitted electron beam (Fig. 1d). For a weak phase object, center-of-mass (CoM) images are directly related to the gradient of the sample electrostatic potential, and DPC images are formed by inverting the differential equation to plot the phase change of the electron probe (Dekkers & De Lang, 1974; Waddell & Chapman, 1979; Lazić et al., 2016; Cao et al., 2018; Ishikawa et al., 2018). Figures 1e and 1f show how much more efficiently DPC can capture structural information as compared to ADF with both a small and large electron probe. Ptychography refers to another family of reconstruction techniques that can be used to map the phase of the sample. Ptychography approaches can be used to solve for the probe and deconvolve it from the object to improve resolution and remove aberrations. Despite the benefits of ptychography, this is a more computationally intensive method. Depending on the experiment and sample, either of these phase techniques may be the better approach (Ophus, 2019; Rodenburg & Maiden, 2019; O'Leary et al., 2021b).

In this work, we explore how 4D-STEM can be used to study these interrelated issues of symmetry and defects. Electron microscopy simulations of beam-specimen interactions can be used in combination with experiments to guide data acquisition and analysis (Meyer et al., 2011; Jung et al., 2019; DaCosta et al., 2021; Parker et al., 2022). These methods can also be used for rapid testing of new techniques before experimental realization (Kirkland, 1998; Madsen & Susi, 2021). Here, we use multislice simulations to explore a wide range of virtual detectors in 4D-STEM experiments. In particular, we compare a variety of virtual detectors for detecting local order in two relevant materials, graphene and lead titanate (PbTiO<sub>3</sub>). We test our design on experimental graphene data and show how these detectors can help highlight atomic contrast and defects. We study how beam modification can be used to amplify these defect features. Moreover, the framework we develop for evaluating virtual detectors can be straightforwardly adapted to other challenges, in order to directly detect defects that cause a break in crystal lattice symmetry.

#### **Methods**

#### **Simulations**

Materials for simulations were built from structural files available through the Materials Project (Jain et al., 2013). STEM simulations were performed using the abTEM (Madsen & Susi, 2021) multislice code based on methods laid out by Kirkland (1998). Image reconstructions were performed using custom virtual detectors and the py4DSTEM package (Savitzky et al., 2021). Simulated datasets were created utilizing an acceleration voltage of 80 kV for graphene and 300 kV for PbTiO<sub>3</sub>. Spherical aberrations, defocus, and tilt were included in the construction of the STEM probe where noted. A perfect, aberration-free probe is used as a "control probe." Poisson noise was applied to simulate dose scaled in counts per probe at the end of multislice simulations. Because twodimensional materials need a high number of frozen phonon configurations to converge (DaCosta et al., 2021), graphene simulations were run with 50 frozen phonons, while PbTiO<sub>3</sub> simulations were run with 10, and the standard deviation of the displacement was 0.05 Å. For the 20 mrad convergence angle and 8 mrad convergence angle, the collection angle of the bright-field detector was <22 and <9 mrad, respectively. The ADF detector was 42–100 mrad, with an inner collection angle matching (Ishikawa et al., 2018).

#### **Experimental Data**

Experimental data was used from (Oxley et al., 2021). The data was acquired using a Nion UltraSTEM 100 operated at 60 kV with a convergence angle of 31 mrad. Virtual detectors were applied for image reconstructions using py4DSTEM (Savitzky et al., 2021).

#### Virtual Detector Design

In Figure 2, we explore detectors, beyond conventional approaches. Here, we use both real and complex values in the detectors, which will be represented by the legend shown in Figure 2b. After applying a complex detector, we plot the magnitude of the sum of all pixels to form an image. Comparing images reconstructed with virtual detectors is a straightforward approach for evaluating 4D-STEM experiments—in addition to the low computational cost and high speed of reconstructions, we can compare the signal to noise of images on a percent probe basis, which is a stand-in for electron dose (Ophus et al., 2016).

Analysis of 4D-STEM data is often driven by prior knowledge of the material structure or symmetry (Krajnak & Etheridge, 2020). Based on the rotation symmetry of graphene, we would anticipate that sixfold or threefold detectors would provide meaningful structural information. To evaluate the best detectors for analysis, we turned to principal component analysis (PCA). PCA has been used in other 4D-STEM experiments to guide virtual detector design (Han et al., 2018; Nguyen et al., 2022). Using a simulation of pristine graphene with a 20 mrad convergence angle, we performed PCA analysis on the resulting data (Supplementary Fig. S2). The first component shows the central beam. Components 2 and 3 are similar to x and y CoM virtual detectors, which underscores the effectiveness of these detectors for graphene. Component 4 shows threefold symmetry, which guided the virtual detector design in Figure 2.

### Results and Discussion Versatility of Virtual Detectors

As described above, bright-field imaging (Fig. 2c) is not the most dose-efficient method. Figures 2d and 2e show wedge detectors that were designed with prior knowledge of the symmetry of graphene combined with the PCA approach. Based on Friedel's law (Friedel, 1913), we expect opposite diffracted beams to be the same in magnitude and opposite in phase. Therefore, the intensity alternates in the areas of overlap between the first-order diffracted beams and the central disk. These different signals are highlighted by the "+" and "-" signs in Figure 2a.

When the wedges are aligned with the lattice, as shown in Figure 2d, these signals interfere constructively, leading to strong intensities from atoms. Red and blue spots appear on atomic sites. The contrast from the vacancy is not easily identifiable with this detector due to the similar contrast of the missing atom. When the detector is rotated 30°, scattering from the lattice interfered destructively, so the areas corresponding to a perfect graphene lattice disappear. However,

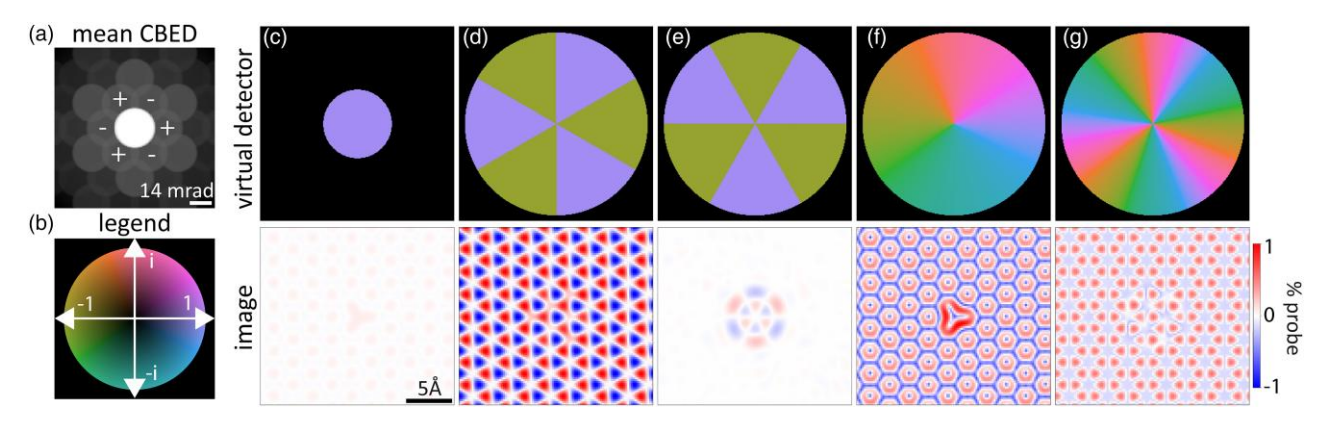


Fig. 2. (a) Graphene mean CBED pattern. (b) Legend for phase and amplitude of virtual detectors and electron beam. (c) Bright-field imaging does not efficiently capture the graphene signal. (d,e) Wedge detectors highlight coherent lattice or defects depending on orientation. (f) Onefold complex detector shows the magnitude of CoM contrast. (g) The threefold complex detectors show atomic positions.

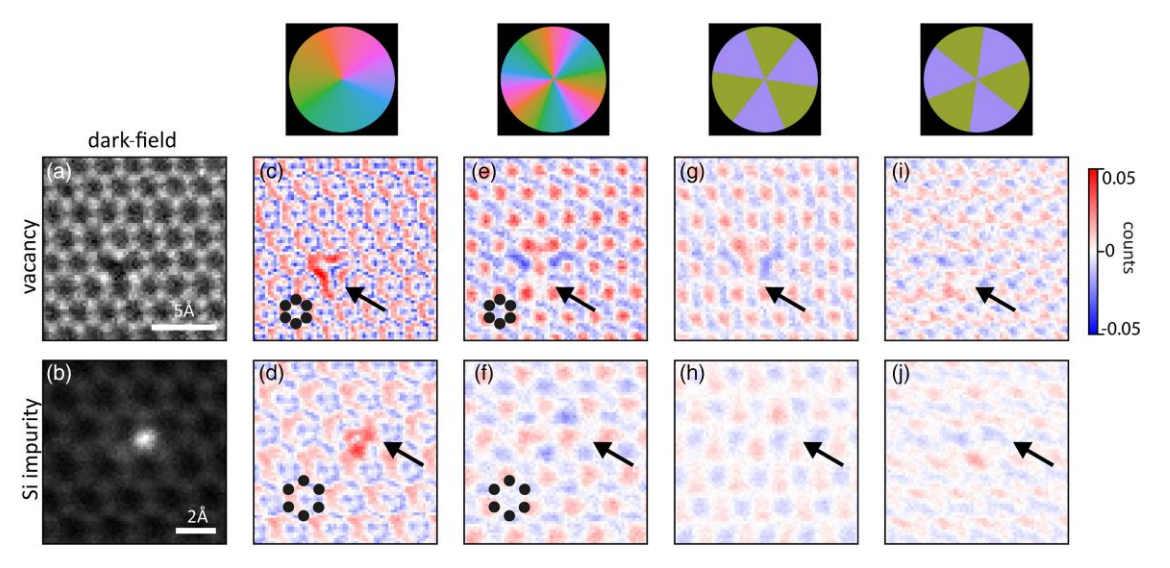


Fig. 3. Graphene with a vacancy and with Si impurity. (a,b) ADF for reference. (c,d) Onefold complex detector shows defect and graphene rings. (e,f) Threefold complex detector highlights graphene atomic positions more clearly than onefold detector. The vacancy appears as missing blue and red contrast. The Si impurity shows slightly higher atomic contrast than the graphene atoms in (f) but is not as clear as in (d). (g,h) When aligned with the lattice, wedge detectors enhance contrast from atomic sites. (i) When the detectors are antialigned, the vacancy appears as missing signal. (j) The Si impurity is highlighted.

the defect breaks long-range order and a strong signal from the missing atom arises. The combination of these detectors provides information about both order and sample orientation.

The magnitude of a onefold complex detector is analogous to the magnitude of a CoM reconstruction. The image resulting from this detector (Fig. 2f) shows a strong signal from both defect and atomic sites. Higher-order rotationally varying detectors provide alternative information about local symmetry. In Figure 2g, we apply a threefold complex detector, which has easier interpretability than the onefold detector and strong signal from the atoms. The vacancy also has threefold symmetry, so it has similar contrast to the atoms in this imaging mode, although we can see small deviations in contrast around the missing atom.

#### Testing with Experimental Data

In order to compare our simulations to experiments, we used 4D data from Oxley et al. (2021) that studies defects in graphene. We used datasets with two different kinds of point

defects, vacancies and Si substitutions. Figures 3a and 3b present the simultaneously acquired ADF images, which we can use to compare against our reconstructions. Figures 3c and 3d show the images from the onefold complex detector. As with the simulated data, this matches the CoM magnitude images. The threefold complex detector (Figs. 3e, 3f) provides a similar signal-to-noise value but more intuitive structural information. The convergence angle used here provides atomic contrast, which is why the strong red and blue contrast from atoms is apparent. It is hard to see the Si impurity, as it is also in a threefold site with atomic contrast, highlighting a limitation of this detector. However, the vacancy is apparent, as we see missing signal at this position.

As shown in Figure 2, images with the wedge detectors have strong rotational dependence. For a dataset with unknown relative rotation between real and reciprocal space, we can use the wedge detectors to solve for the rotation. The signal is maximized with a 8° rotation. The resulting images (Figures 3g and 3h) are similar to the threefold complex detector reconstructions. The images in Figures 2i and 2j have weak

contrast, which is expected given the destructive atomic interference. For the vacancy, we see some signal missing from the defect, and we would expect the defect to be even further highlighted in an experiment with a smaller convergence angle.

#### Understanding a Large Design Space

Figure 2 proposes a number of detectors that can be used to highlight structural information from graphene, but ultimately the image contrast will change with experimental conditions. To determine how robust the contrast is with these detectors, we scored our images based on the signal from the defect versus the background signal, using masks defined in Supplementary Figure S3,

$$SNR = \frac{\mu_{|defect|} - \mu_{|lattice|}}{\sigma_{|lattice|}}$$
 (1)

To help make the trends more apparent to the reader, we plot the square root of SNR here, with more red squares scoring higher. This scheme gives high marks to images like those in Figure 4b, where the defect is highlighted above atomic signals. It also gives low scores to images like those in Figure 2c, where contributions from the atomic lattice dominate the contrast. This is a beneficial visualization technique in a system like graphene where the lattice is well defined, and one would be interested in quickly and efficiently finding breaks in symmetry.

By testing the detectors described in Figure 2 against a variety of experimental parameters, we observe that the CoM type detector with a relative small convergence angle (8 mrad) is the most consistently efficient way to highlight a defect (Fig. 4d). This can be explained by the fact that with a small convergence angle, or large probe in real space, the 4D-STEM experiment is less sensitive to variations in atomic contrast, making other signals more apparent. This result is also the most robust against commonly encountered aberrations, such as spherical aberrations and defocus.

For atomic resolution images, such as those in Figure 2, aberrations and defocus will interfere with the ability to resolve atomic information. Although these results are obtained for graphene, this suggests that this rotationally varying detectors and a small convergence angle can be used to highlight defects that break long-range order in other systems as well.

#### Amplifying Signal with Beam Modification

Modifying the phase or amplitude of an electron beam before interaction with the sample can also dramatically influence image contrast. In TEM experiments, especially for imaging of weak phase objects such as biological molecules, a Zernike or Volta phase plate is routinely used to enhance image contrast (Danev & Baumeister, 2017; Wang & Fan, 2019). In STEM, it has been shown that modification of the probe by inserting a phase plate in the probe-forming aperture enhances the signal from both heavy and light elements across a wide range of spatial frequencies (Ophus et al., 2016).

Combining the concepts of phase plates and wedge detectors, we can evaluate the impact of beam modification on image contrast. In Figures 5a and 5b, we show the same images as Figures 2d and 2e but with a 10× larger contrast range. The signal from the aligned lattice is significantly reduced, and it is no longer easy to see the defect.

In Figures 5c-5f, we explore how modifying the incident beam can improve the information transfer from this defect. On the left, the phase and amplitude of the electron beam is

plotted, and then to its right are images with two different virtual detectors. Especially in Figures 5c and 5f, we can see how matching detectors and beams can highlight the atomic signal or the defect contrast. The obtained signal from the defect in these images is higher than without beam modification, which leads to a more efficient characterization approach.

Although phase plates provide an exciting avenue for improving image contrast, they are difficult to implement experimentally (Malac et al., 2021). Therefore, we turned to testing this approach with vortex beams, as they have been demonstrated in both TEM and STEM with a variety of beam modification mechanisms (Uchida & Tonomura, 2010; Verbeeck et al., 2010; McMorran et al., 2011; Verbeeck et al., 2012). Vortex beams carry orbital angular momentum, and this probe is independent of the material or crystal orientation, allowing for much broader applicability. The wavefunction of a vortex beam,  $\Psi_{\nu}(q)$ , is defined by

$$\Psi_{\nu}(q) = \Psi(q) e^{im\phi} \tag{2}$$

Here,  $\Psi(q)$  is the wavefunction of an unmodified beam, m is the quantum number, and  $\phi$  is the azimuthal coordinates with respect to the propagation direction of the electron beam. Figure 5g shows a vortex beam in real and reciprocal space with m=1. We observe enhanced contrast from the vortex beam—for example, comparing Figures 5h and 5i, we see stronger intensity and a more localized signal. Figure 5h shows the same control as 5b, namely, the virtual detectors with a control probe. However, here the contrast is scaled to a lower value because the vortex beam is not as efficient as a beam with threefold phase contrast. Although this is not as high transfer of information as with the tailored probe in Figure 5f, the vortex beam provides an improvement in defect detection with reduced beam modification challenges.

There are other benefits to using an electron vortex beam when studying symmetry, as they are not bound by Friedel's law (Juchtmans et al., 2016). In Figure 6a, we highlight graphene's symmetry. The atomic sites have threefold symmetry, as highlighted with purple bars, while the voids between atoms have sixfold symmetry, as shown in green. Both of these sites have sixfold symmetry in reciprocal space, as demonstrated in the diffraction patterns in Figures 6b and 6c. We can compare these to CBED patterns taken from the same locations but with a vortex beam (Figs. 6d, 6e). Here, we see that the atomic site has threefold diffraction symmetry, while the void is sixfold. This experiment highlights the benefits of using the vortex beam to probe symmetry.

Krajnak & Etheridge (2020) introduced the concept of symmetry STEM or S-STEM. In this dose-efficient method, the image is based on the cross-correlation between a CBED pattern and the same pattern after a symmetry operation has been applied. This is a powerful method to understand crystalline order and has been suggested as an effective tool to look for vacancies and other defects. We explore an extension of this approach to map symmetry using the vortex beam.

The S-STEM maps are effective for highlighting both the graphene structure and the defect. There is a large signal-to-noise difference between the vortex and the control beam for twofold symmetry (Figs. 6f, 6i). The vortex case produces a stronger signal and highlights the defect.

We can explore higher symmetries, which will also be different for the conventional and vortex probes. As shown in Figures 6g and 6j, the threefold S-STEM images show bright contrast at all the atomic sites. The vacancy also has threefold

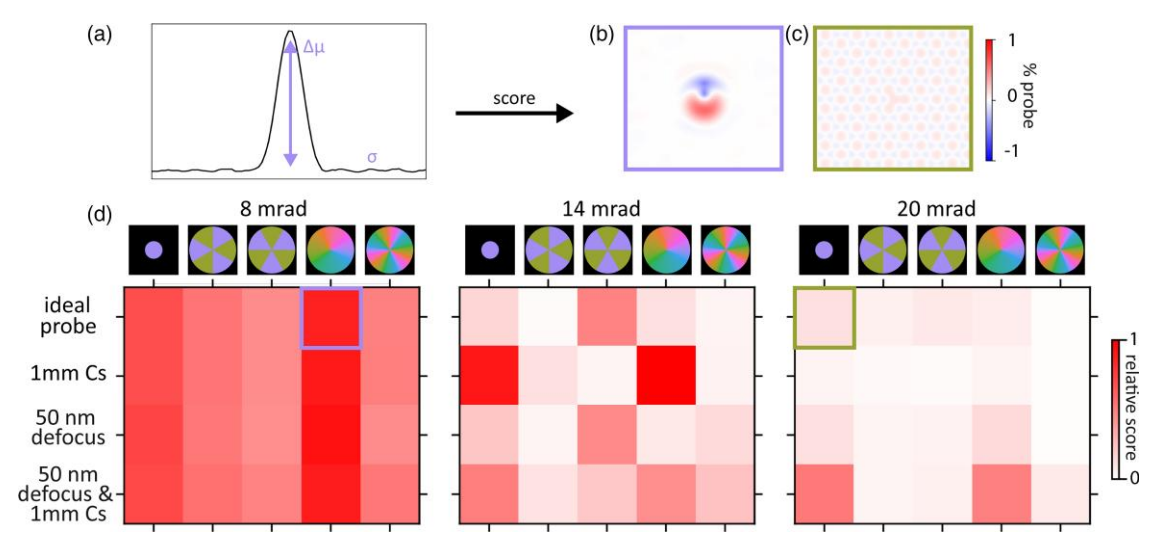
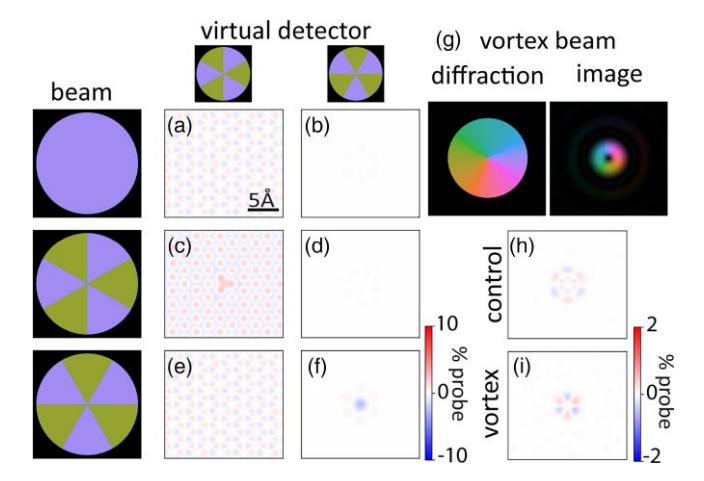


Fig. 4. (a) The scoring metric evaluates the signal to noise of the defect, which gives high marks to (b) with the defect highlighted above the atomic signal as compared to (c) where we see atomic contrast. (d) Square root of SNR: testing across a range of experimental parameters and detectors suggests small convergence angle and a rotationally varying detector is the best way to highlight the defect.



**Fig. 5.** With an ideal probe, the wedge shape detectors show (a) atomic and (b) defect contrast depending on orientation. However, if the beam is modified before interaction with the sample (c)–(f), the contrast is stronger. In (c,f), the virtual detectors and beam modification are matched. (c) Shows holes in graphene rings and the vacancy, while (f) shows only the defect. (g) A vortex beam can also enhance the signal from the defect as shown in (i) as compared to (h).

symmetry, so it appears similarly to the atomic sites. With the control beam, we see slightly reduced intensity from the neighboring atoms around the vacancy, as they are no longer in a threefold environment. This contrast difference is amplified in the vortex beam case (Fig. 6j).

The higher sixfold symmetry map has weak contrast with the control probe. With the vortex probe, we can observe the faint sixfold spots between atoms. Supplementary Figure S4 shows these results across a wider range of convergence angles and symmetries. Overall S-STEM provides a powerful tool to map symmetry in 4D-STEM experiments, and a vortex beam could provide a way to make this technique even more interpretable.

#### **Beyond 2D Materials**

Two-dimensional systems, such as graphene, are ideal for testing new virtual detectors and beam modification in 4D-STEM experiments. However, many key materials science challenges are in understanding structures that do not have an inherently two-dimensional architecture. Towards that end, we show simulations of 15 nm PbTiO<sub>3</sub>, a bulk material, which is known to undergo a ferroelectric ordering transition (Shirane & Hoshino, 1951). We can use the virtual detector design rules established with graphene to see how well they translate to another structure with more complex scattering. Based on our results in Figure 4, we use a small convergence angle (2 mrad) and apply similar detectors as shown in Figure 2.

We explore the PbTiO<sub>3</sub> structure with two-dimensional defects, or domain walls (Nataf et al., 2020), to test the virtual detectors. In our model structure (Fig. 7a), the heavy lead atoms are aligned, but the low-Z titanium and oxygen atoms are lined up in opposite directions creating four local domains with two different types of dipoles. There are three types of domain walls in this structure: head-to-head, tail-to-tail, and opposite orientation.

The bright-field image (7b) identifies the head-to-head and tail-to-tail domain boundaries. These walls have a larger difference in atomic density as compared to the bulk structure, which makes them easier to see with bright-field. The opposite orientation domain boundaries are harder to detect.

In Figure 7c, we can see that segmented detectors more efficiently pick up on all the domain boundaries, and Figure 7d shows intensity from the opposite-facing domain walls. The onefold rotationally varying detector (Fig. 7e) provides domain orientation information, as the upward and downward-facing domains have different contrast.

The onefold center complex detector provides comparable contrast to the magnitude of CoM images. In this sample, the PbTiO<sub>3</sub> has minimal *y* deflection, so the dominant contrast in this image matches the x-component of the CoM images, as shown in Supplementary Figure S5. The twofold rotationally varying detector (Fig. 7f) highlights the defects and differentiates between the different kinds of domain boundaries. Overall virtual detectors (Figs. 7c–7f) provide helpful correlative information to conventional approaches for identifying defects.

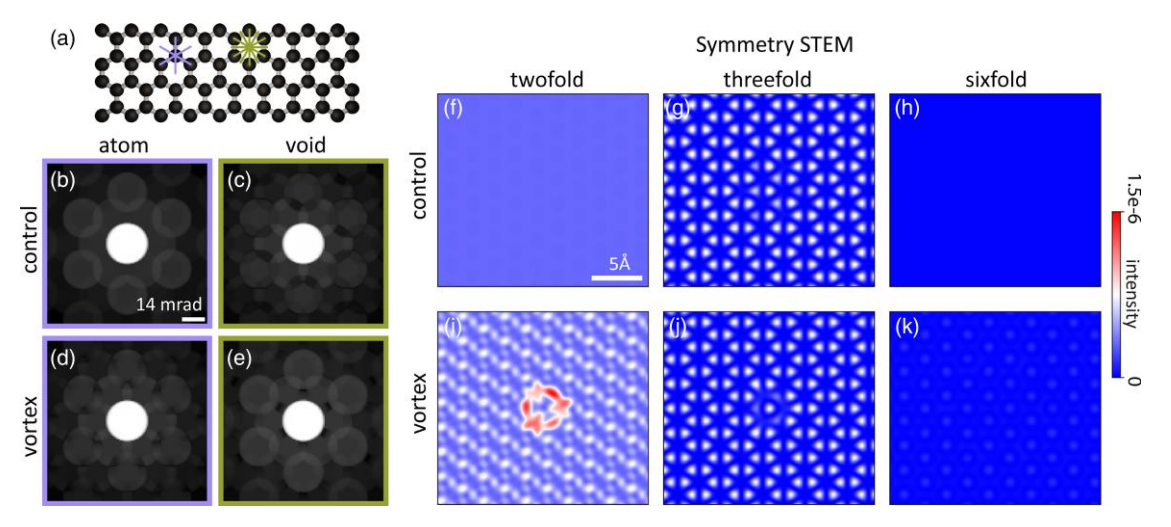
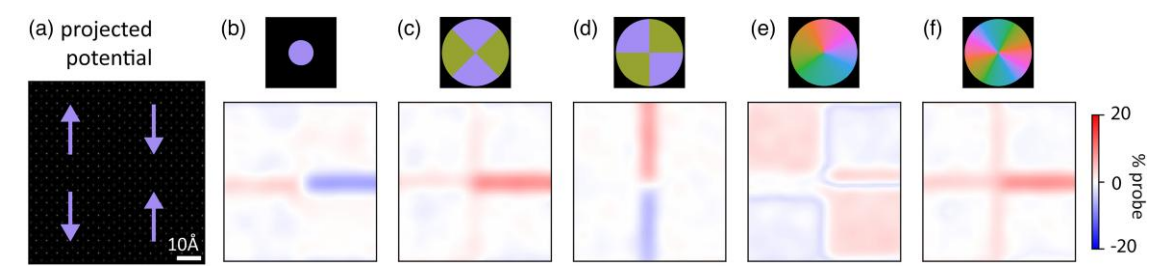


Fig. 6. (a) Graphene atomic sites and voids have threefold and sixfold symmetry, respectively, which (b,c) appear as sixfold symmetry in CBED patterns. (d,e) the vortex beam distinguishes between three and sixfold symmetry as the diffraction pattern from the atomic position now has threefold instead of sixfold symmetry. (f)—(k) Both probes can be used for finding atomic positions and defects with S-STEM. However, the vortex beam lends itself especially well to S-STEM maps for finding defects, as demonstrated in the twofold case (i).



**Fig. 7.** (a) PbTiO<sub>3</sub> sample with ferroelectric domain boundaries. (b) Bright-field imaging picks up on some walls. (c,d) Wedge-shaped detectors accentuate boundaries. (e) Complex detector highlights the different phases of domains. (f) Twofold complex detector shows all boundaries.

One potential challenge in applying virtual detectors in PbTiO<sub>3</sub> is the possibility for contrast reversals based on thickness and tilt (Shao et al., 2019; Zeltmann et al., 2022). To that end, we perform simulations on a variety of thicknesses and mistilts. Supplementary Figure S6 shows simulations of the same sample but at 1.5 and 2 times thickness (23 and 31 nm, respectively). The wedge detectors have the most consistent contrast and pickup on the boundaries between domains. Supplementary Figure S7 explores how large mistilts of the beam can change the contrast in the image. These simulations are with the same 15 nm sample and up to 5 mrad of tilting. As with the variations in thickness, there are some contrast reversals, but for the most part, these detectors can pickup on the boundaries. Careful simulations and calibrations would be needed to compare against experiments. However, overall these images suggest that correlative images from different detectors could be helpful for finding defected areas of interest for further study.

#### **Summary and Outlook**

In this work, we explored the use of beam modification and virtual detectors to enhance contrast from defects in 4D-STEM experiments. In systems such as graphene and PbTiO<sub>3</sub>, where the structure is well characterized, we are most interested in elevating the defect signal above other contrast. We have shown how using a small convergence angle

and a rotationally varying detector most efficiently finds these features. This study focuses on crystalline materials, although in the future, we are interested in understanding how these ideas can be extended to less ordered systems. Moreover, the framework used here to evaluate images can be extended in future studies aimed at scoring approaches for materials characterization. We aim to continue exploring the large design space of virtual detectors to highlight material properties.

This study also tests electron beam profiles beyond the conventional probe. There are many practical experimental challenges to phase and amplitude modification of an electron beam (Malac et al., 2021), with only further complications in an experiment as proposed in Figure 5, where the orientation of the probe relative to the sample modifies contrast. We plan continued investigation into phase and amplitude plates, both in experiment and simulation.

#### **Availability of Data and Materials**

Simulation data is available on Zenodo.

#### **Supplementary Material**

To view supplementary material for this article, please visit https://doi.org/10.1093/micmic/ozad045.

#### **Acknowledgments**

We thank Steven Zeltmann for helpful feedback on this manuscript.

#### **Financial Support**

This material is based upon work supported by the U.S. Department of Energy, Office of Science, Office of Workforce Development for Teachers and Scientists, Office of Science Graduate Student Research (SCGSR) program. The SCGSR program is administered by the Oak Ridge Institute for Science and Education for the DOE under contract number DE-SC0014664. S.M.R. acknowledges support from the IIN Ryan Fellowship and the 3M Northwestern Graduate Research Fellowship. This material is based upon work supported by the National Science Foundation under Grant No. DMR-1929356. CO acknowledges support from the US Department of Energy Early Career Research Program. This work made use of the EPIC facility of Northwestern University's NUANCE Center, which has received support from the SHyNE Resource (NSF ECCS-2025633), the International Institute of Nanotechnology (IIN), and Northwestern's MRSEC program (NSF DMR-1720139). Work at the Molecular Foundry was supported by the Office of Science, Office of Basic Energy Sciences, of the U.S. Department of Energy under contract number DE-AC02-05CH11231.

#### **Conflict of Interest**

The authors declare that they have no competing interest.

#### References

- Araujo P, Tvand Terrones M & Dresselhaus MS (2012). Defects and impurities in graphene-like materials. *Mater Today* **15**(3), 98–109.
- Arslan Irmak E, Liu P, Bals S & Van Aert S (2021). 3D atomic structure of supported metallic nanoparticles estimated from 2D ADF STEM images: A combination of atom-counting and a local minima search algorithm. *Small Methods* 5(12), 2101150.
- Bustillo KC, Zeltmann SE, Chen M, Donohue J, Ciston J, Ophus C & Minor AM (2021). 4D-STEM of beam-sensitive materials. Acc Chem Res 54(11), 2543–2551.
- Cao MC, Han Y, Chen Z, Jiang Y, Nguyen KX, Turgut E, Fuchs GD & Muller DA (2018). Theory and practice of electron diffraction from single atoms and extended objects using an EMPAD. *Microscopy* 67(suppl\_1), i150-i161.
- Chen Q, Dwyer C, Sheng G, Zhu C, Li X, Zheng C & Zhu Y (2020). Imaging beam-sensitive materials by electron microscopy. *Adv Mater* 32(16), 1907619.
- DaCosta LR, Brown HG, Pelz PM, Rakowski A, Barber N, O'Donovan P, McBean P, Jones L, Ciston J, Scott MC & Ophus C (2021). Prismatic 2.0 Simulation software for scanning and high resolution transmission electron microscopy (STEM and HRTEM). *Micron* 151, 103141.
- Dahmen U, Erni R, Radmilovic V, Ksielowski C, Rossell M-D & Denes P (2009). Background, status and future of the transmission electron aberration-corrected microscope project. *Philos Trans R Soc A* 367-(1903), 3795–3808.
- Danev R & Baumeister W (2017). Expanding the boundaries of cryo-EM with phase plates. Curr Opin Struct Biol 46, 87–94.
- Dekkers N & De Lang H (1974). Differential phase contrast in a STEM. *Optik* 41(4), 452–456.
- DiStefano JG, Murthy AA, Hao S, Dos Reis R, Wolverton C & Dravid VP (2020). Topology of transition metal dichalcogenides: The case of the core-shell architecture. *Nanoscale* 12(47), 23897–23919.

- Egerton R & Watanabe M (2022). Spatial resolution in transmission electron microscopy. *Micron* 160, 103304.
- Fatermans J, Den Dekker A, Müller-Caspary K, Lobato I, O'Leary C, Nellist P & Van Aert S (2018). Single atom detection from low contrast-to-noise ratio electron microscopy images. *Phys Rev Lett* 121(5), 056101.
- Friedel G (1913). Sur les symétries cristallines que peut révéler la diffraction des rayons röntgen. C R Acad Sci Paris 157, 1533–1536.
- Geim AK & Novoselov KS (2007). The rise of graphene. *Nat Mater* 6(3), 183–191.
- Haas B, Mittelberger A, Meyer C, Plotkin-Swing B, Dellby N, Krivanek O, Lovejoy T & Koch C (2021). High-fidelity 4D-STEM enabled by live processing at 15,000 detector frames per second. *Microsc Microanal* 27(S1), 994–997.
- Han Y, Nguyen K, Cao M, Cueva P, Xie S, Tate MW, Purohit P, Gruner SM, Park J & Muller DA (2018). Strain mapping of two-dimensional heterostructures with subpicometer precision. *Nano Lett* 18(6), 3746–3751.
- Huang PY, Ruiz-Vargas CS, Van Der Zande AM, Whitney WS, Levendorf MP, Kevek JW, Garg S, Alden JS, Hustedt CJ, Zhu Y, *et al.* (2011). Grains and grain boundaries in single-layer graphene atomic patchwork quilts. *Nature* **469**(7330), 389–392.
- Ishikawa R, Findlay SD, Seki T, Sánchez-Santolino G, Kohno Y, Ikuhara Y & Shibata N (2018). Direct electric field imaging of graphene defects. *Nat Commun* 9(1), 1–6.
- Jacoboni C, Canali C, Ottaviani G & Quaranta AA (1977). A review of some charge transport properties of silicon. Solid State Electron 20(2), 77–89.
- Jain A, Ong SP, Hautier G, Chen W, Richards WD, Dacek S, Cholia S, Gunter D, Skinner D, Ceder G & Persson K a. (2013). The materials project: A materials genome approach to accelerating materials innovation. APL Mater 1(1), 011002.
- Juchtmans R, Guzzinati G & Verbeeck J (2016). Extension of Friedel's law to vortex-beam diffraction. *Phys Rev A* **94**(3), 033858.
- Jung HJ, Bao J-K, Chung DY, Kanatzidis MG & Dravid VP (2019). Unconventional defects in a quasi-one-dimensional KMn6Bi5. Nano Lett 19(10), 7476–7486.
- Kirkland EJ (2010). Advanced Computing in Electron Microscopy, 2nd ed. New York, NY: Springer.
- Krajnak M & Etheridge J (2020). A symmetry-derived mechanism for atomic resolution imaging. Proc Natl Acad Sci USA 117(45), 27805–27810.
- Krivanek OL, Chisholm MF, Nicolosi V, Pennycook TJ, Corbin GJ, Dellby N, Murfitt MF, Own CS, Szilagyi ZS, Oxley MP, et al. (2010). Atom-by-atom structural and chemical analysis by annular dark-field electron microscopy. Nature 464(7288), 571–574.
- Lazić I, Bosch EG & Lazar S (2016). Phase contrast STEM for thin samples: Integrated differential phase contrast. *Ultramicroscopy*, 160, 265–280.
- Liu X, Farahi G, Chiu C-L, Papic Z, Watanabe K, Taniguchi T, Zaletel MP & Yazdani A (2022). Visualizing broken symmetry and topological defects in a quantum hall ferromagnet. *Science* 375(6578), 321–326.
- Madsen J, Liu P, Kling J, Wagner JB, Hansen TW, Winther O & Schiøtz J (2018). A deep learning approach to identify local structures in atomic-resolution transmission electron microscopy images. Adv Theory Simul 1(8), 1800037.
- Madsen J & Susi T (2021). The abTEM code: Transmission electron microscopy from first principles. *Open Res Europe* 1(24), 24.
- Malac M, Hettler S, Hayashida M, Kano E, Egerton RF & Beleggia M (2021). Phase plates in the transmission electron microscope: Operating principles and applications. *Microscopy* 70(1), 75–115.
- McMorran BJ, Agrawal A, Anderson IM, Herzing AA, Lezec HJ, McClelland JJ & Unguris J (2011). Electron vortex beams with high quanta of orbital angular momentum. *Science* 331(6014), 192–195.
- Meyer JC, Kurasch S, Park HJ, Skakalova V, Künzel D, Groß A, Chuvilin A, Algara-Siller G, Roth S, Iwasaki T, *et al.* (2011). Experimental analysis of charge redistribution due to chemical

bonding by high-resolution transmission electron microscopy. *Nat Mater* **10**(3), 209–215.

- Nataf G, Guennou M, Gregg J, Meier D, Hlinka J, Salje E & Kreisel J (2020). Domain-wall engineering and topological defects in ferroelectric and ferroelastic materials. Nat Rev Phys 2(11), 634–648.
- Nguyen KX, Huang J, Karigerasi MK, Kang K, Cahill DG, Zuo J-M, Schleife A, Shoemaker DP & Huang PY (2023). Angstrom-scale imaging of magnetization in antiferromagnetic Fe2 as via 4D-STEM. *Ultramicroscopy* **247**, 113696.
- O'Leary CM, Haas B, Koch CT, Nellist PD & Jones L (2022). Increasing spatial fidelity and SNR of 4D-STEM using multi-frame data fusion. *Microsc Microanal* 28(4), 1417–1427.
- O'Leary CM, Martinez GT, Liberti E, Humphry MJ, Kirkland AI & Nellist PD (2021). Contrast transfer and noise considerations in focused-probe electron ptychography. *Ultramicroscopy* **221**, 113189.
- Ophus C (2019). Four-dimensional scanning transmission electron microscopy (4D-STEM): From scanning nanodiffraction to ptychography and beyond. *Microsc Microanal* 25(3), 563–582.
- Ophus C, Ciston J, Pierce J, Harvey TR, Chess J, McMorran BJ, Czarnik C, Rose HH & Ercius P (2016). Efficient linear phase contrast in scanning transmission electron microscopy with matched illumination and detector interferometry. *Nat Commun* 7(1), 1–7.
- Ophus C, Shekhawat A, Rasool H & Zettl A (2015). Large-scale experimental and theoretical study of graphene grain boundary structures. *Phys Rev B* **92**(20), 205402.
- Oxley MP, Ziatdinov M, Dyck O, Lupini AR, Vasudevan R & Kalinin SV (2021). Probing atomic-scale symmetry breaking by rotationally invariant machine learning of multidimensional electron scattering. *npj Comput Mater* 7(1), 1–6.
- Parker KA, Ribet S, Kimmel BR, Dos Reis R, Mrksich M & Dravid VP (2022). Scanning transmission electron microscopy in a scanning electron microscope for the high-throughput imaging of biological assemblies. *Biomacromolecules* 23(3), 3235–3242.
- Philipp HT, Tate MW, Shanks KS, Mele L, Peemen M, Dona P, Hartong R, van Veen G, Shao Y-T, Chen Z, Thom-Levy J, Muller DA & Gruner SM (2022). Very-high dynamic range, 10,000 frames/second pixel array detector for electron microscopy. *Microsc Microanal* 28(2), 425–440.
- Plotkin-Swing B, Haas B, Mittelberger A, Dellby N, Hotz M, Hrncirik P, Meyer C, Zambon P, Hoermann C, Meffert M, Bachevskaya D, Piazza L, Krivanek OL & Lovejoy TC (2022). 100,000 diffraction patterns per second with live processing for 4D-STEM. *Microsc Microanal* 28(S1), 422–424.
- Ribet SM, Murthy AA, Roth EW, dos Reis R & Dravid VP (2021). Making the most of your electrons: Challenges and opportunities in characterizing hybrid interfaces with STEM. *Mater Today* 50, 100–115.
- Rodenburg J & Maiden A (2019). Ptychography. In *Springer Handbook* of *Microscopy*, Hawkes PW & Spence JCH (Eds.), pp. 819–904. Cham: Springer Nature.
- Savitzky BH, Zeltmann SE, Hughes LA, Brown HG, Zhao S, Pelz PM, Pekin TC, Barnard ES, Donohue J, DaCosta LR, Kennedy E, Xie Y, Janish MT, Schneider MM, Herring P, Gopal C, Anapolsky A, Dhall R, Bustillo KC, Ercius P, Scott MC, Ciston J, Minor AM &

- Ophus C (2021). py4DSTEM: A software package for four-dimensional scanning transmission electron microscopy data analysis. *Microsc Microanal* 27(4), 712–743.
- Shao Y-T, Chen Z, Mei A, Holtz M, Padgett E, Schlom D & Muller DA (2019). Decoupling polarization, crystal tilt and symmetry in epitaxially-strained ferroelectric thin films using 4D-STEM. *Microsc Microanal* 25(S2), 1938–1939.
- Shirane G & Hoshino S (1951). On the phase transition in lead titanate. *J Phys Soc Japan* 6(4), 265–270.
- Smith BW & Luzzi DE (2001). Electron irradiation effects in single wall carbon nanotubes. *J Appl Phys* **90**(7), 3509–3515.
- Spiegelberg J, Idrobo JC, Herklotz A, Ward TZ, Zhou W & Rusz J (2018). Local low rank denoising for enhanced atomic resolution imaging. *Ultramicroscopy* 187, 34–42.
- Sun Y, Abtew TA, Zhang P & Zhang S (2014). Anisotropic polaron localization and spontaneous symmetry breaking: Comparison of cation-site acceptors in GaN and ZnO. *Phys Rev B* 90(16), 165301.
- Tate MW, Purohit P, Chamberlain D, Nguyen KX, Hovden R, Chang CS, Deb P, Turgut E, Heron JT, Schlom DG, *et al.* (2016). High dynamic range pixel array detector for scanning transmission electron microscopy. *Microsc Microanal* 22(1), 237–249.
- Uchida M & Tonomura A (2010). Generation of electron beams carrying orbital angular momentum. *Nature* 464(7289), 737–739.
- Van Aert S, Batenburg KJ, Rossell MD, Erni R & Van Tendeloo G (2011). Three-dimensional atomic imaging of crystalline nanoparticles. *Nature* 470(7334), 374–377.
- Van Swygenhoven H & Weertman JR (2006). Deformation in nanocrystalline metals. *Mater Today* 9(5), 24–31.
- Verbeeck J, Tian H & Béché A (2012). A new way of producing electron vortex probes for STEM. *Ultramicroscopy* **113**, 83–87.
- Verbeeck J, Tian H & Schattschneider P (2010). Production and application of electron vortex beams. *Nature* **467**(7313), 301–304.
- Waddell E & Chapman J (1979). Linear imaging of strong phase objects using asymmetrical detectors in STEM. *Optik* 54, 83–96.
- Wang H-W & Fan X (2019). Challenges and opportunities in cryo-EM with phase plate. *Curr Opin Struct Biol* 58, 175–182.
- Zeltmann SE, Hsu S-L, Brown HG, Susarla S, Ramesh R, Minor AM & Ophus C (2022). Uncovering polar vortex structures by inversion of multiple scattering with a stacked Bloch wave model. arXiv, arXiv:2211.05842, preprint.
- Zeng H, Leburton J-P, Xu Y & Wei J (2011). Defect symmetry influence on electronic transport of zigzag nanoribbons. *Nanoscale Res Lett* **6**(1), 1–6.
- Zhang C, Han R, Zhang AR & Voyles PM (2020). Denoising atomic resolution 4D scanning transmission electron microscopy data with tensor singular value decomposition. *Ultramicroscopy* 219, 113123.
- Zheng Y, Slade TJ, Hu L, Tan XY, Luo Y, Luo Z-Z, Xu J, Yan Q & Kanatzidis MG (2021). Defect engineering in thermoelectric materials: What have we learned? *Chem Soc Rev* 50, 9022–9054.
- Ziatdinov M, Dyck O, Maksov A, Li X, Sang X, Xiao K, Unocic RR, Vasudevan R, Jesse S & Kalinin SV (2017). Deep learning of atomically resolved scanning transmission electron microscopy images: Chemical identification and tracking local transformations. ACS Nano 11(12), 12742–12752.